

# Accuracy and Composability in NODAS

Gilbert C. Wong<sup>1</sup>, Gerard K. Tse<sup>1</sup>, Qi Jing<sup>3</sup>, Tamal Mukherjee<sup>1</sup>, Gary K. Fedder<sup>1,2</sup>

<sup>1</sup>Department of Electrical and Computer Engineering and <sup>2</sup>The Robotics Institute  
Carnegie Mellon University  
Pittsburgh, PA USA

<sup>3</sup>Mentor Graphics Corporation  
Wilsonville, OR USA

## Abstract

Simulation accuracy of a methodology for composable modeling of microelectromechanical systems (MEMS) is assessed by comparing against analytic equations and finite element simulations. Several MEMS canonical problems are composed hierarchically as networks of simple elements with models written in an analog hardware description language. Schematics built from this model library, called NODAS (NODal Design of Actuators and Sensors), produce DC simulation results that are accurate to at least three digits, demonstrating suitable accuracy and lumping trade-offs.

## I. Introduction

MEMS designers rely on analytic equations and finite element simulations to design their devices. Analytic equations allow the designer to find a ballpark solution, which is refined using a finite element package. However, with the integration of MEMS devices and CMOS circuits, the designer requires a simulation environment for the system. NODAS [1] is a set of lumped element electromechanical models developed at Carnegie Mellon University which can perform this function. NODAS uses the Verilog-A hardware modeling language [2] and can be simulated using Cadence's Spectre simulator [3]. This paper focuses on DC accuracy as a step toward a comprehensive analysis of the NODAS models for use in accurate time domain simulation of MEMS. Prior work in MEMS modeling have included SUGAR from UC Berkeley [4] [5], Coventor Architect [6] [7], and [8].

In order to produce a physically accurate model of a MEMS device, the structural representation of the physical system is broken down into a network of atomic elements. Each atomic element is a behavioral model which describes how the element reacts to external stimuli. The NODAS library contains three atomic elements: beams, plates and electrostatic gaps. Each element has a 2D or 3D model, with the exception of the gap element, which has currently only a 2D model [1]. Based on Kirchoff's flow law, nodal analysis can be performed on these elements by ensuring that the sum of forces and moments into a node is zero, which is equivalent to performing force and moment balance. Complex MEMS structures can be composed using these elements.

RF MEMS devices is an area which has generated much research recently. RF switches which utilize both cantilever beams (Fig. 1a) [9] and fixed-fixed beams (Fig. 1b) [10] [11] have been demonstrated. Possible applications include wireless devices such as cell phones and switching networks for satellite systems. RF filters utilizing cantilever beams [12] and RF mixers and mixer-filters using fixed-fixed beams [13] have also been demonstrated. These passive MEMS mixers offer a low power alternative to active circuit mixers in transceivers. MEMS filters can replace discrete off-chip components with on-chip devices.

Simulation of RF MEMS devices brings two challenges to the AHDL-based circuit-level simulation approach used in SUGAR, Architect, and NODAS. The first is the preponderance of nonlinear models due to the large displacements relative to the size of the MEMS device. The second is the dominance of distributed nature of the physical forces.

NODAS nonlinear beam and electrostatic gap models have been derived in [1] (beam models are based on [15]). [1] contains the Verilog-A code for these models. Both of these elements have nonlinearities in the force equations. The nonlinear beam model includes geometric effects of large deflections and nonlinear stiffening or softening from axial stress. The NODAS electrostatic gap model is augmented with a physics-based contact model (needed to simulate an RF switch) in Section II. The distributed modeling challenge is addressed by decomposing (discretizing) the beam and gap representing the RF MEMS device in the rest of the paper. Canonical MEMS modeling problems of the cantilever (Section III) and fixed-fixed (Section IV) beams that dominate RF MEMS designs are then discussed. The cantilever beam problem tests the large geometric deflection accuracy in the nonlinear beam model. The fixed-fixed beam problems test the accuracy in handling large axial stress. A fixed-guided-end canonical problem is developed in Section

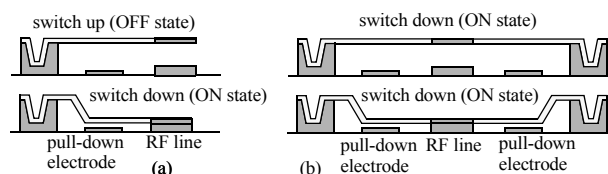


Figure 1: (a) Cantilever and (b) Fixed-fixed RF MEMS switch structure.

IV to model the residual stress in the beams arising from the thin-film manufacturing processes. Though these RF MEMS devices use electrostatic actuation, both pure mechanical actuation and electrostatic actuation are explored in order to demonstrate the accuracy of the NODAS beam and gap models separately. For verification, all NODAS simulation results are compared with analytic equations and FEMLAB [14] in each section.

## II. Electrostatic Gap Contact Model

When a voltage is applied between two electrodes, the electrostatic force between them pulls them together. In the case of an RF switch, one of the electrodes is anchored to the substrate, while the other electrode is the moving beam. The restoring force of the beam, arising from the beam's stiffness, resists the electrostatic force. When the voltage is increased, a point is reached where the electrostatic force equals the spring restoring force of the beam. If this point, known as pull-in voltage, is passed, the beam will snap to the substrate.

To ensure that the moveable electrode does not travel beyond the anchored electrode, the gap contact model applies a stiff restoring spring contact force to oppose the electrostatic force when the electrodes come in contact. Our previous model for this contact force was a process dependent linear spring model [16]. Fig. 2a shows the load line plot for the  $1/g^2$  relationship of the electrostatic force plotted against the restoring linear spring force of the contact model. The electrostatic force is a family of curves which increases as the voltage is increased. A mathematical artifact of this inverse square relationship is that there may be multiple solutions. Two physical solutions (one stable, and one unstable) are present in the first quadrant as well as one stable non-physical

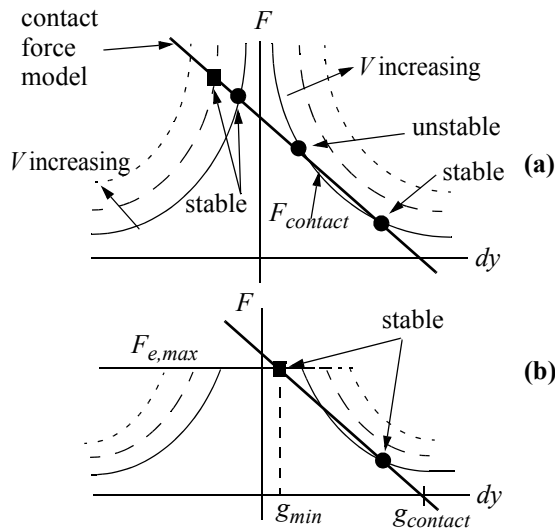


Figure 2: (a) Contact and electrostatic force plotted against  $dy$ , the gap between the two electrodes, (b) modified contact force equation to ensure first quadrant solution.

cal solution occurs in the second quadrant (filled black circles in the figure) for low voltages. When the voltage is increased, the only remaining stable solution is in the non-physical second quadrant (black square in the figure).

To remedy the non-physical solution, the gap contact model must guarantee that a stable first quadrant solution exists when in contact. To ensure this, the current contact model (described in Fig. 2b) limits the applied electrostatic force using a process specific electric field breakdown parameter,  $E_{max}$ . This is used to compute  $F_{e,max}$ , the maximum electrostatic force per unit length defined as:  $F_{e,max} = -0.5 * \epsilon_0 * thickness * E_{max}^2$ , where  $\epsilon_0$  is the permittivity of free space. The contact force is a straight line from  $(g_{min}, F_{e,max})$  to  $(g_{contact}, 0)$ , where  $g_{min}$  is a user-specified minimum allowed gap and  $g_{contact}$  is the point when the beams first come into contact. At  $dy \geq g_{contact}$  ( $dy$  is the dynamic gap between the electrodes), the contact force is 0. When  $dy < g_{contact}$ , the linear contact force model becomes active (second if/else block in Fig. 3b). Additionally, the electrostatic force per unit length,  $F_{elec}$ , is constrained to be less than  $F_{e,max}$  (first if/else block in Fig. 3b). As seen in Fig. 2b, by constraining  $F_{elec} \geq F_{e,max}$  and by requiring that the contact force model pass through the point  $(g_{min}, F_{e,max})$ , the non-physical second quadrant solution cannot occur. Fig. 3a shows a schematic of two beams with the variables mentioned in Fig. 3b.

Equation 1 is the lumping integral for node  $a$ , the left node of beam 1 (Fig. 3a).  $f_{11}(x)$  is the beam basis function used to lump the force to node  $a$ .  $Fl$  is the electric field per unit length, which will be either  $F_{e,max}$  or  $F_{elec}$ . A rotated parallel plate model, with an angle  $\theta_0$  with respect to the local frame, is assumed for the calculation of the electrostatic forces and the lumping integral is performed in this rotated frame. Fig. 4 shows the Verilog-A code for the eight force and moment lumping equations. A rotation matrix is applied to the calculated lumped forces in the rotated frame of reference to translate them into forces in the local frame of reference:  $Fb1y, Fa1y, Fa2y, Fb2y$ .

$$Fa11 = \int_{-\frac{\theta v}{2}}^{\frac{\theta v}{2}} f_{11}(x) \cdot Fl \cdot dx \quad (1)$$

Fig. 5a shows a test case used to verify the gap contact model. A rigid electrode connected to an ideal spring with  $K=0.68$  N/m, is constrained to only move in the  $y$  direction. A piece-wise linear voltage source which sweeps from 0 V to 100 V and back to 0 V was used. Fig. 5b shows the  $y$  displacement of the movable electrode plotted against applied voltage. When the moveable electrode traverses 1/3 of the gap, it snaps to the anchor. Note that a hysteresis exists such

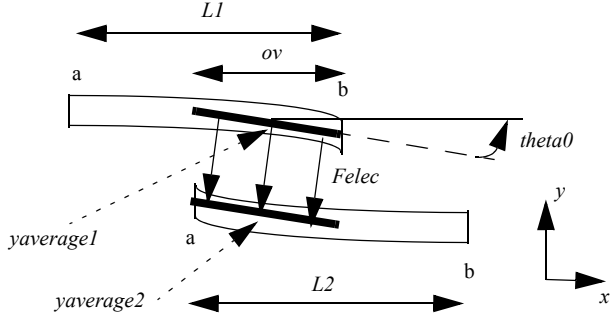


Figure 3: (a) The rotated parallel plate approximation showing some variables used in the Verilog-A code.

```

// The parallel plate force in the overlap region
// rotated by angle theta0. The force is constant through this region
// force per unit length
Felec = -0.5*eps0*thickness*v_squared/
pow((cos(theta0)*(y1average-y2average)),2);

// Maximum electric field, based on the electric field breakdown
// force per unit length
FeMax = -0.5*eps0*thickness*pow(elec_breakdown,2);

// if the electric force per unit length
// is greater than the max electric force, set the force/l to FeMax
if (abs(Felec) > abs(FeMax)) begin
    Fl = FeMax;
end
else begin
    Fl = Felec;
end

// slope of the contact force
// must multiply by ov because FeMax is the force per unit length
slope = -(FeMax*ov)/(gmin - gcontact);

// the contact force
if (dy < gcontact) begin
    // contact force
    Fy_contact = slope*(dy-gcontact);
end
else begin
    // there is a normal gap, no contact
    Fy_contact = 0;
end

```

*Felec* is the electric field per unit length. *FeMax* is the maximum electric field per unit length. *eps0* is the permittivity of free space. *thickness* is the thickness of the beam. *v\_squared* is the applied voltage squared. *theta0* is the rotation angle of the parallel plate. *elec\_breakdown* is a process parameter which sets the maximum electric field. The default is 100 V/ $\mu$ m. *Fl* is a variable used to store *Felec* or *FeMax*, depending on which one is smaller. *Fl* is used in the integrand of the lumping integral. *gmin* is the minimum gap allowed. *gcontact* is the point when the beams first come in contact. *dy* is the dynamic gap. *Fy\_contact* is the equation of the contact force model.

Figure 3: (b) Verilog-A code for the contact model.

that even when decreasing the voltage past the original pull-in voltage, the electrodes remain in contact.

```

// The following 8 equations are lumped forces and moments
// we must rotate the force Fl to the y direction in the local frame
Fa1_l = -Fl*(2*L1-ov)*pow(ov,3)/(2*pow(L1,3));
Ma1_l = -Fl*(4*L1-3*ov)*pow(ov,3)/(12*pow(L1,2));
Fb1_l = -Fl*(ov-pow(ov,3)/pow(L1,2)+pow(ov,4)/(2*pow(L1,3)));
Mb1_l = -Fl*(-pow(ov,2)*(6*pow(L1,2)-8*L1*ov+3*pow(ov,2))/
12*pow(L1,2));
Fa2_l = Fl*(ov-pow(ov,3)/pow(L2,2)+pow(ov,4)/(2*pow(L2,3)));
Ma2_l = Fl*(-pow(ov,2)*(6*pow(L2,2)-8*L2*ov+3*pow(ov,2))/
(12*pow(L2,2)));
Fb2_l = Fl*(2*L2-ov)*pow(ov,3)/(2*pow(L2,3));
Mb2_l = Fl*(4*L2-3*ov)*pow(ov,3)/(12*pow(L2,2));

```

// Rotate the forces back into the local frame

```

Fa1y = sin(theta0)*0+cos(theta0)*Fa1l;
Fb1y = sin(theta0)*Fxdl+cos(theta0)*Fb1l;
Fa2y = sin(theta0)*(-Fxdl)+cos(theta0)*Fa2l;
Fb2y = sin(theta0)*0+cos(theta0)*Fb2l;

```

Figure 4: Verilog-A code showing one of eight force and moment lumping equations. *theta0* is the angle that the rotated parallel plate gap model makes with the local frame, *L1* is the length of the top beam, *L2* is the length of the bottom beam, *ov* is the dynamic overlap. *Fl* was defined in Fig. 3, and is either  $F_{e,max}$  or  $F_{elec}$ .

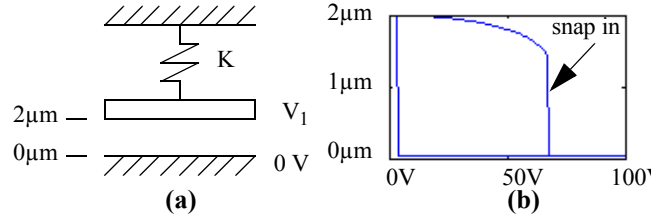


Figure 5: DC sweep simulation showing snap-in characteristics and hysteresis. (a) Snap-in test case,  $l=20\mu\text{m}$ ,  $w=t=2\mu\text{m}$ ,  $E=170\text{GPa}$ ,  $\rho=2330\text{kg/m}^3$ ,  $K=0.68\text{N/m}$ , (b) DC sweep from 0V-100V and from 100V-0V showing the *y* displacement of the movable electrode.

### III. Cantilever Beam

The cantilever beam is a basic MEMS structure where one end of the beam is fixed and the other end is unconstrained. Fig. 6. illustrates two loading cases: a uniformly distributed load,  $q$ , in the *y* direction (Fig. 6a) and spatially varying load,  $q_e(x)$ , from electrostatic force with gap voltage,  $V$  (Fig. 6b).

All simulations are performed with beams 100  $\mu\text{m}$  long, 2  $\mu\text{m}$  wide, and 2  $\mu\text{m}$  thick. The Young's modulus was set to 170 GPa and the density was set to 2330  $\text{kg/m}^3$ , representative of a polysilicon MEMS process. NODAS simulations used 2, 4, 8, 16 and 32 beam elements. Fig. 6c shows a cantilever beam split into 4 segments. Fig. 7 shows the mode shapes of the cantilever beam with 0 V, 40 V, and 80 V applied between the electrodes. At 40 V, the cantilever beam has not snapped in yet. The 80 V plot shows the snapped in cantilever beam. Note that for this simulation, the NODAS linear beam was used because the gap model cannot currently handle large geometric deflections in the *y* direction, which will cause a potentially large *x* deflection.

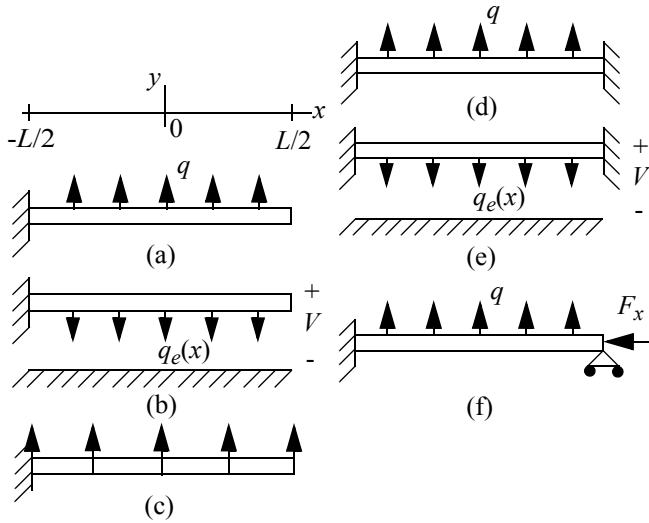


Figure 6: Canonical beam problems. (a) cantilever, uniform distributed load, (b) cantilever, electrostatic actuation, (c) fixed-fixed beam, uniform distributed load, (d) fixed-fixed beam, electrostatic actuation, (e) guided-end beam, uniform distributed load with axial force,  $F_x$ , (f) a cantilever beam split into 4 segments.

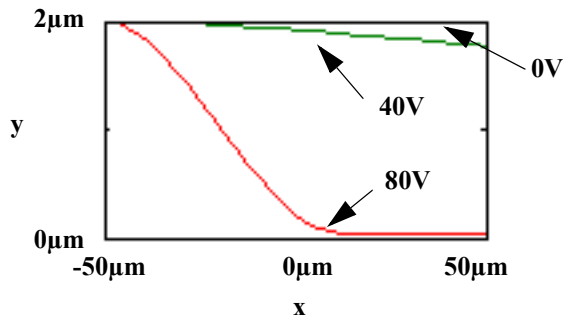


Figure 7: Cantilever beam mode shapes. The y displacement is shown with  $0\text{V}$ ,  $40\text{V}$  and  $80\text{V}$  applied between the two electrodes. 32 beam segments used.  $w=t=2\mu\text{m}$ ,  $L=100\mu\text{m}$ ,  $E=170\text{GPa}$ ,  $\rho=2330\text{ kg/m}^3$ . NODAS linear beam used.

Simulations for electrostatic actuation with  $10\text{ V}$  across the gap are compared against FEMLAB, a finite-element package. The results are presented in Fig. 8 as a percentage difference in the  $y$  displacement versus the  $x$  position along the beam. Using only two beam elements results in a 13% difference between NODAS and FEMLAB. In order to get an idea of where the error might be coming from, a pure mechanical simulation with a uniform distributed load is considered in Fig. 9. This simulation results in a significant, but smaller, 8% difference between NODAS and FEMLAB.

Two conclusions can be made. First, when a distributed force, such as an electrostatic force, is applied at discrete points along the beam, some information is lost on how the real forces act on the beam. However, the composibility of the NODAS models can be used to improve the accuracy of the results. As shown, when 8 or more beam elements are

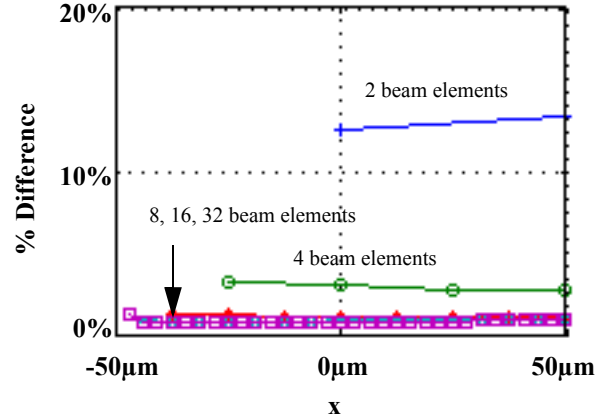


Figure 8:  $y$  displacement of a cantilever beam with electrostatic actuation at  $10\text{ V}$ . NODAS vs. FEMLAB.  $\% \text{Difference} = 100 \cdot (1 - y_{\text{NODAS}}/y_{\text{FEMLAB}})$ . 2, 4, 8, 16, and 32 beam elements plotted.  $w=t=2\mu\text{m}$ ,  $L=100\mu\text{m}$ ,  $E=170\text{GPa}$ ,  $\rho=2330\text{ kg/m}^3$ .

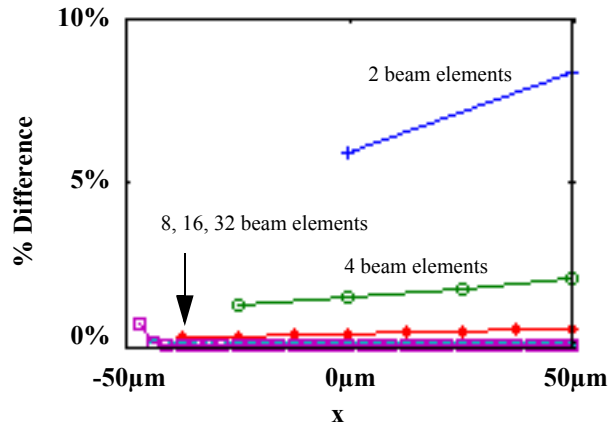


Figure 9:  $y$  displacement of a cantilever beam with a  $50\text{ nN}$  distributed load. NODAS vs. FEMLAB.  $\% \text{Difference} = 100 \cdot (1 - y_{\text{NODAS}}/y_{\text{FEMLAB}})$ . 2, 4, 8, 16, and 32 beam segments plotted.  $w=t=2\mu\text{m}$ ,  $l=100\mu\text{m}$ ,  $E=170\text{GPa}$ ,  $\rho=2330\text{ kg/m}^3$ .

used, the difference between NODAS and FEMLAB drops below 1% in both the pure mechanical and electrostatic simulations. In the case of the pure mechanical simulation, the difference is even less. When using 8 beam elements, the error is below 0.5% and when using 32 beam elements, the difference is below 0.06%. By using more beam elements, distributed force can be more accurately modeled.

Second, the current implementation of the gap model introduces additional error into the solution. It assumes that the beam electrodes are parallel plates defined by straight plane electrodes between the segment's nodes (Fig. 3a). It is obvious that if only two gap elements are used, there would be a significant error since two straight beam electrode segments were created. However, due to the composibility of the NODAS gap element, more gaps and beams can be added to increase the accuracy. The parallel plate approximation is still used, but each parallel plate is smaller, and if enough

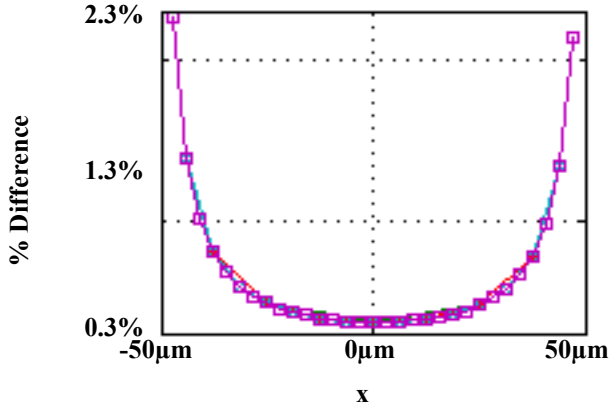


Figure 10: y displacement of a fixed-fixed beam with a 50nN uniform distributed load. NODAS vs. FEMLAB. %Difference =  $100 \cdot (1 - y_{\text{NODAS}}/y_{\text{FEMLAB}})$ . 2, 4, 8, 16, and 32 beam segments plotted.  $w=t=2\mu\text{m}$ ,  $l=100\mu\text{m}$ ,  $E=170\text{GPa}$ ,  $\rho=2330\text{ kg/m}^3$ .

gap elements are included, the electrostatic forces can be accurately modeled. In the 32 beam/gap element simulation, the difference between NODAS and FEMLAB results range between 1.17% near the fixed end of the beam to 0.83% near the free end of the beam. Placing 32 gap and beam elements is cumbersome, and if more accuracy is needed, even more beam elements can be placed.

#### IV. Fixed-Fixed Beam

The fixed-fixed beam (Fig. 6d and e) is a topology which MEMS designers use to build high resonant frequency structures. As the name implies, both ends of the beams are fixed, thus constraining the ends of the beams to zero displacement and zero angle. Two loading cases of the fixed-fixed beam will be considered: a uniformly distributed load  $q$ , in the  $y$  direction (Fig. 6d), and a spatially varying load,  $q_e(x)$ , from electrostatic force with gap voltage,  $V$  (Fig. 6e).

DC simulation results of the fixed-fixed beam with a 50 nN uniformly distributed load are compared to the analytic solution, without including shearing forces, match with 8 digit precision at all nodes along the beam length. However, when the results are compared to FEMLAB (Fig. 10), the difference between the NODAS simulation and FEMLAB is greater. The difference is not due to convergence of the finite element analysis as refining the mesh did not alter the results of the FEMLAB simulation. Enabling the NODAS shear model reduces the difference between NODAS and FEMLAB at the ends of the beams to less than 1%. Fig. 11 shows the comparison of NODAS with FEMLAB for an electrostatically actuated fixed-fixed beam. The accuracy is similar to the uniform distributed load case, implying that the accuracy may not be limited by the electrostatic force model.

Fig. 12 shows the mode shape of the fixed-fixed beam with electrostatic actuation for three voltages: 320 V, 140 V, and

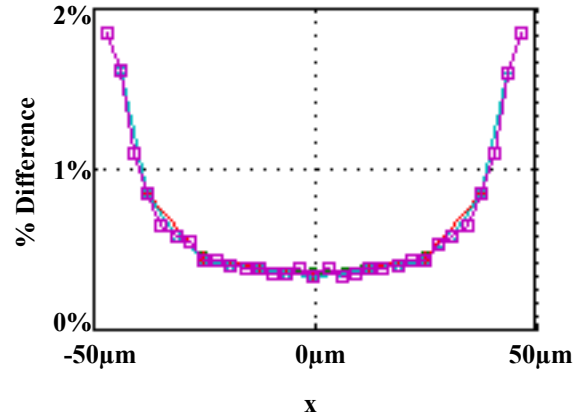


Figure 11: y displacement of a fixed-fixed beam with electrostatic actuation. NODAS vs. FEMLAB.  $V_1 - V_2 = 10\text{V}$ . %Difference =  $100 \cdot (1 - y_{\text{NODAS}}/y_{\text{FEMLAB}})$ . 2, 4, 8, 16, and 32 beam segments plotted.  $w=t=2\mu\text{m}$ ,  $l=100\mu\text{m}$ ,  $E=170\text{GPa}$ ,  $\rho=2330\text{ kg/m}^3$ .

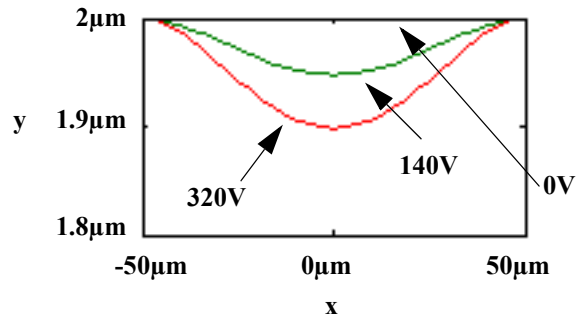


Figure 12: Fixed-fixed beam mode shapes. The y displacement is shown with 0V, 140V and 320V applied between the two electrodes. 32 beam segments used.  $w=t=2\mu\text{m}$ ,  $L=100\mu\text{m}$ ,  $E=170\text{GPa}$ ,  $\rho=2330\text{ kg/m}^3$ . NODAS nonlinear beam used.

0 V. The simulator was not able to converge at the snap-in point. As mentioned previously, the large geometric deflections, which occur in the fixed-fixed beams, is not handled in the current gap model, but will be addressed in the next version of the model.

Microfabrication of fixed-fixed beams with thin-film materials lead to residual axial stress, which alters the characteristics of the beam. The fixed-guided topology can be used to simulate these stress effects. Fig. 6f shows a picture of a fixed-guided-end beam. As the name implies, one end of the beam is fixed but the other end is allowed to move only in the  $x$  direction. The analytic solution and the NODAS simulation agree within 0.0015%.

#### V. Conclusion

The design of RF integrated circuits incorporating MEMS devices such as cantilever switches and fixed-fixed beam resonator filters requires the ability to simulate the mechanical, electrostatic, and contact physical behavior with transistor electronics. A physical contact force model is combined

with the existing NODAS nonlinear electrostatic gap model and the NODAS nonlinear beam model. Cantilever, fixed-fixed, and fixed-guided-end simulation models of the RF switches and filters are developed in NODAS. The simulation models include various levels of schematic discretization. Results from NODAS simulation are compared with analytic equations and FEMLAB simulation to evaluate composability and accuracy. These results demonstrate the applicability of using network simulation to represent structures with simple AHDL-based physics models for the simulation of MEMS involving distributed physical systems dominant in RF MEMS applications.

### Acknowledgements

This research effort is sponsored by the Defense Advanced Research Projects Agency (DARPA) and US Army CECOM under agreement number DAAB07-02-C-K001 and in part by the Pittsburgh Digital Greenhouse.

### VI. References

- [1] Q. Jing, *Modeling and Simulation for Design of Suspended MEMS*, Ph.D thesis, Carnegie Mellon University, 2003. (<http://www.ece.cmu.edu/~mems/pubs/>)
- [2] *Affirma Verilog-A Language Reference*, Version 4.4.6, Cadence Design Systems, Inc., San Jose, CA, 2001.
- [3] *Affirma Spectre Circuit Simulator User Guide*, Version 4.4.6, Cadence Design Systems, Inc., San Jose, CA, 2000.
- [4] J. V. Clark, N. Zhou, S. Brown and K.S.J. Pister, "Nodal Analysis for MEMS Simulation and Design", *1998 Int. Conf. on Modeling and Simulation of Microsystems, Semiconductors, Sensors and Actuators (MSM '98)*, Santa Clara, CA, April 6-8, 1998.
- [5] J. V. Clark, N. Zhou, S. Brown, and K.S.J. Pister, "MEMS Simulation Using SUGAR v0.5," *1998 Solid-State Sensors and Actuators Workshop*, Hilton Head Is., SC, June 7-11, 1998, pp. 191-196.
- [6] R. Neul, G. Lorenz and S. Dickmann, "Modeling and Simulation of Microelectromechanical Sensor Systems," *Microtec 2000*.
- [7] Coventor Architect: <http://www.coventor.com/coventorware/architect/>
- [8] D. Teegarden, G. Lorenz and R. Nuel, "How to Model and Simulate Microgyroscope Systems," *IEEE Spectrum*, pp. 67-75, July 1998.
- [9] S. Majumder, J. Lampen, R. Morrison and J. Maciel, "A Packaged, High-Lifetime Ohmic MEMS RF Switch," *Microwave Symposium Digest*, pp. 1935-1938, June 8-13, 2003.
- [10] N.S. Barker, G.M. Rebeiz, "Distributed MEMS True-Time Delay Phase Shifters And Wide-Band Switches," *Microwave Theory and Techniques*, pp. 1881-1890, Nov. 1998.
- [11] G.-L. Tan, G.M. Rebeiz, "A DC-Contact MEMS Shunt Switch," *Microwave and Wireless Components Letters*, pp. 212-214, June 2002.
- [12] E. Fourn, C. Quendo, E. Rius, A. Pothier, P. Blondy, C. Champeaux, J.C. Orlianges, A. Catherinot, G. Tanne, C. Person, F. Huret, "Bandwidth And Central Frequency Control On Tunable Bandpass Filter By Using MEMS Cantilevers," *Microwave Symposium Digest*, pp 523-526, June 8-13, 2003.
- [13] C.T.-C. Nguyen, "Transceiver Front-End Architectures Using Vibrating Micromechanical Signal Processors," *Silicon Monolithic Integrated Circuits in RF Systems*, pp. 23-32, Sept. 12-14 2001.
- [14] FEMLAB, <http://www.femlab.com/>.
- [15] J.S. Przemieniecki, *Theory of Matrix Structural Analysis*, McGraw-Hill, New York, New York, 1968.
- [16] Q. Jing, T. Mukherjee and G. K. Fedder, "Schematic-Based Lumped Parameterized Behavioral Modeling for Suspended MEMS," in *Proc. ACM/IEEE International Conference on Computer Aided Design (ICCAD '02)*, San Jose, CA, November 10-14, 2002, pp. 367-373.
- [17] G. Lorenz and R. Neul, "Network-Type Modeling of Micromachined Sensor Systems," *1998 Int. Conf. on Modeling and Simulation of Microsystems, Semiconductors, Sensors and Actuators (MSM '98)*, Santa Clara, CA, April 6-8, 1998.
- [18] J. Vandemeer, M.S. Kranz, and G. K. Fedder, "Nodal Simulation of Suspended MEMS with Multiple Degrees of Freedom," *1997 Int. Mechanical Engineering Congress and Exposition: The Winter Annual Meeting of ASME in the 8th Symposium, on Microelectromechanical Systems (DSC-Vol. 62)*, Dallas, TX, 16-21 November, 1997, pp. 113-118.